

Supporting Information for
"Enhanced Second-Order Nonlinearities at
Strained Ultrasharp Zigzag Edges in
Multilayer MoS₂"

Adrián Dewambrechies,^{†,‡,§} Alexander Yu. Polyakov,^{†,¶,§} Betül Küçüköz,[†] and
Timur O. Shegai^{*,†}

[†]*Department of Physics, Chalmers University of Technology, 412 96 Göteborg, Sweden*

[‡]*Current address: Freie Universität Berlin, Department of Physics, 14195 Berlin, Germany*

[¶]*SMENA Catalysis AB, 412 96 Göteborg, Sweden*

[§]*These authors contributed equally.*

E-mail: timurs@chalmers.se

S1. Second Harmonic Generation setup

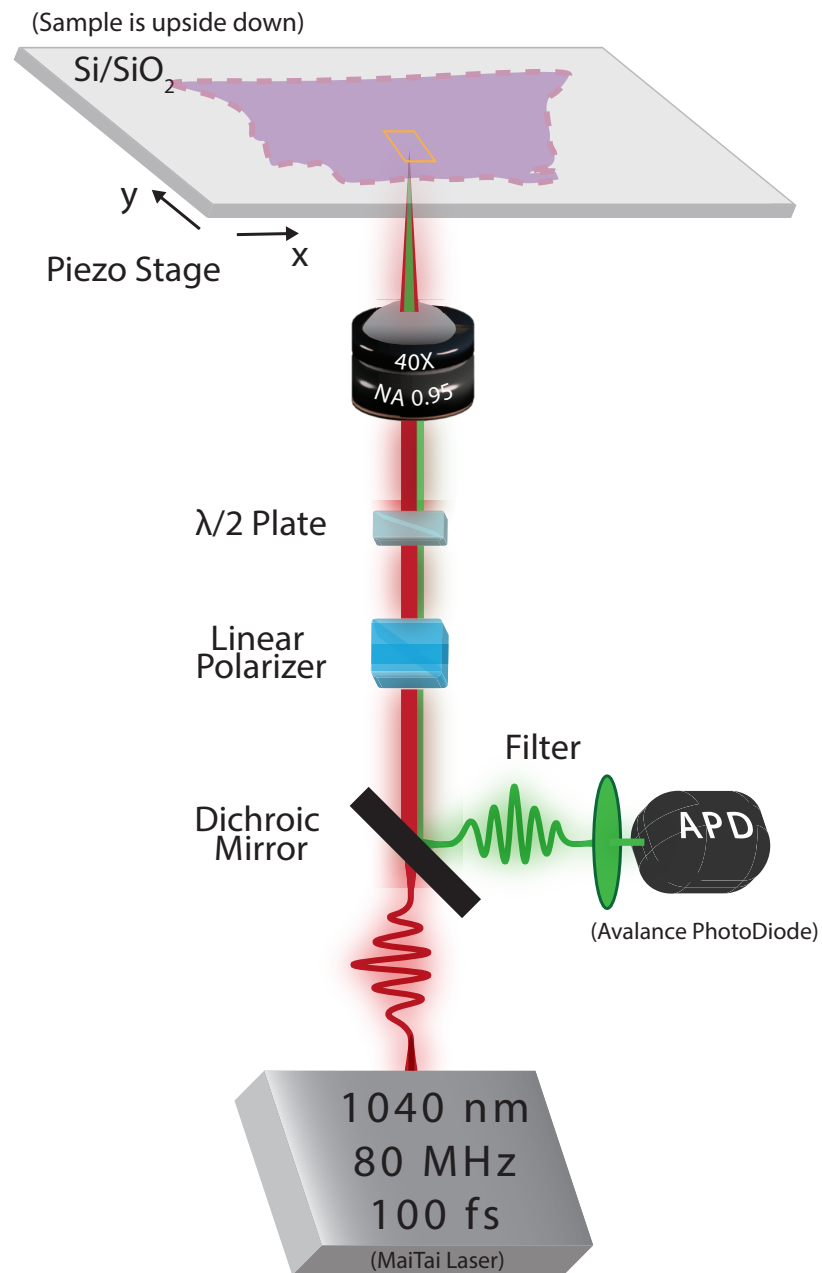


Figure S1: Schematic of the Second Harmonic Generation setup described in the Main text, Section 2.2.

S2. Additional optical and SEM images of the samples

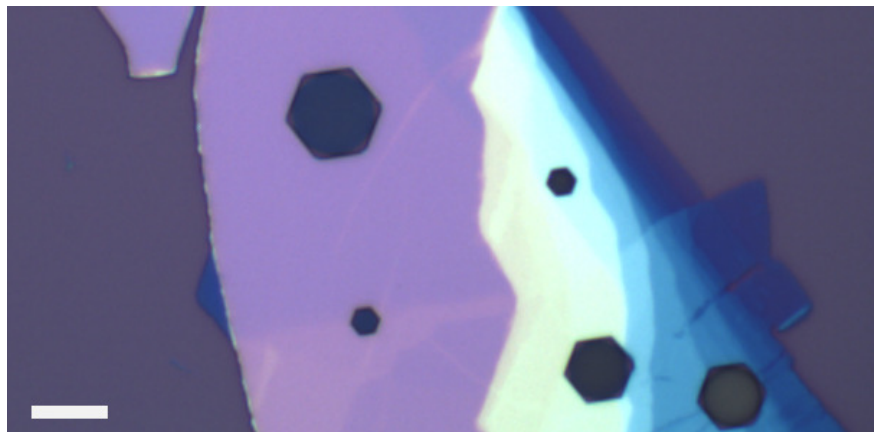


Figure S2: Optical image of hexagonal etching pits in WS₂. The scale bar is 10 μm .

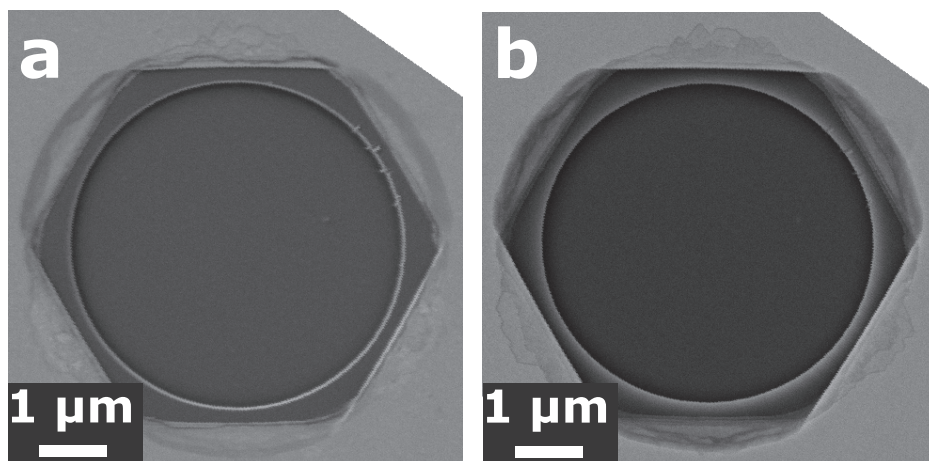
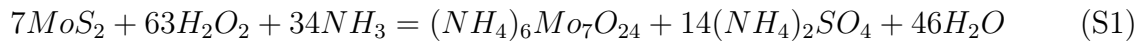


Figure S3: SEM images of the same MoS₂ 5 μm hexagon recorded at 1 kV (a) and 5 kV (b) e-beam accelerating voltages, respectively. Note that the 5 μm hexagon is etched in the same flake as the 2 μm (discussed in the Main text) and therefore shares the same stacking faults and polytype intergrowths.

S3. Chemical aspects of H₂O₂-based wet etching

The wet etching mixture applied in this work is essentially oxidative: H₂O₂ acts as an oxidant (including indirect reactions *via* generation of molecular oxygen and hydroperoxyl radicals), while an aqueous ammonia solution facilitates the dissolution and removal of oxidized Mo-containing by-products in the form of ammonium molybdate species. The process can be described by the following idealized equation:



H₂O₂ withdraws electrons from MoS₂ and leaves molybdenum and sulfur moieties of higher oxidation state (most probably, Mo⁺⁵, Mo⁺⁶, and S⁺⁶) in a solid disulfide. Formation of these moieties is more expected near the sites of H₂O₂ attack, which are at the edges of the growing etching pits. Considering relatively large multilayer flakes instead of monolayers, a certain conductivity of semiconducting MoS₂ can lead to a generation of more oxidized atoms virtually at any site of the flake's surface. In this way, *p*-doping can be introduced to the entire MoS₂ flake upon the spontaneous redox reaction with H₂O₂. To restore the initial electron balance of the disulfide, the oxidized species must be removed from it. Sulfate fragments can be dissolved/removed easier, while NH₃·aq is required to facilitate the complexation and dissolution of molybdate species. Still, complete elimination seems to be harder to achieve. Therefore we can hypothesize that wet-etching used here can introduce a certain *p*-doping to the MoS₂ flakes and leave oxidized species, predominantly, Mo-containing (hydr)oxide moieties, on the very edges of the etching pits.

S4. MoS₂ *zz* edges termination at different etching conditions

Direct identification of Mo/S-*zz* edge terminations of the triangular etching pits by scanning transmission electron microscopy (STEM) or scanning tunneling microscopy (STM) is significantly less mature than in CVD-grown MoS₂ islands research. The discussion about termination tends to be limited to generalities and comparisons with other works, often neglecting to consider the differences in the chemical environment. S-terminated triangles were assumed in the case of 2D etching of the top layer in MoS₂ flakes by water steam.^{S1} Mo-termination was claimed when monolayer MoS₂ was etched by annealing in 41% O₂/Ar.^{S2} However, for a pretty similar etching (annealing in the air), S-termination was predicted by density functional theory (DFT).^{S3} According to DFT calculations, Mo-*zz* energy drops monotonically during oxidation by O₂, while there is a plateau for S-*zz*, which might make it the slowest etched edge.^{S3} Direct edge visualization was performed by annular dark field STEM for a triangular etching pit in the MoS₂ bilayer with parallel stacking.^{S4} These pits were fabricated by a two-step etching process: O₂ plasma dry etching through a mask (created by a block copolymer lithography) was followed by wet etching in a diluted potassium ferricyanide solution. Mo-*zz* were found to border the etching pits.^{S4} Recently Huang *et al.* used an integrated differential phase contrast STEM for direct observation of the edge termination in the thermally etched monolayer WS₂.^{S5} It was corroborated by the etching pits' orientation *vs.* the initial WS₂ monolayer single crystal (CVD-grown) and also proven for monolayer MoS₂ and WSe₂. The etching pits were also fabricated in two steps: 300-400 nm circular holes were made by laser irradiation in ambient air and then thermally etched at 1000°C in a controlled atmosphere. It was unequivocally demonstrated that tuning the chemical gas composition upon thermal etching enables controllable changing of the metal-*zz* and chalcogen-*zz* edge stability. In Ar/H₂ atmosphere, triangular etching pits were bordered by metal-*zz* edges, while Ar/S (Se) vapor atmosphere resulted in triangles with

chalcogen-*zz* edges. Hexagonal etching pits formed in the Ar atmosphere had alternating metal-*zz* and chalcogen-*zz* edges^{S5} ^a. Note that regardless of the *crystallographic* edge orientation/termination, the *real structure* of the very edge can be composed of guest atoms like oxygen and amorphized regions resulting from the etching process, which deteriorate the edge properties.^{S6} For example, electron energy loss spectroscopy in the STEM regime (STEM-EELS) found an oxygen signal in the edge region of H₂O₂-etched WS₂.^{S7} An amorphized layer or adsorbed by-products can be seen on STEM images of MoS₂ edges formed *via* treatment with potassium ferricyanide^{S4} and WS₂ edges formed by high-temperature annealing.^{S5} Still, the tendency to incorporate guest atoms or amorphized moieties might differ between S-*zz* and Mo-*zz* edges.

S5. Difference between wet etching of MoS₂ and WS₂

Stabilization of sharp hexagonal etching pits occurs when all the edges containing an armchair component are etched out significantly faster than i-*zz* ones. Like in the case of the monolayer discussed above, the free energy difference between crystal faces composed of *ac* and i-*zz* will affect the stability of the etching pit shape. If the etching rate difference is large, the *ac* faces are consumed fast, and i-*zz* faces self-limit the etching process. Such a self-limiting behavior was observed upon both WS₂ wet-etching by H₂O₂-containing solution^{S7} and reactive ion etching by SF₆ plasma.^{S8} On the other hand, if the etching rates of the *ac* and *zz* edges differ less, it will take longer for the crystal structure to change the initial circular shape of the etching pit into a crystallography-defined hexagon, and the final shape will be less sharp. We hypothesize that the energy difference between *ac* and *zz* edges in MoS₂ is smaller than in WS₂ upon oxidative H₂O₂-based wet etching. Therefore, the etching pits in WS₂ are much sharper and have less distorted morphology compared to the ones in MoS₂. Similarly, the final hexagon walls in WS₂ always stay closer to the initial dry-etched circle of a given size

^aThis study also indicates that MoS₂ can be etched in a reducing (Ar/H₂) and inert (Ar) atmosphere once the atoms in the MoS₂ structure are affected by high thermal energies. Conversely, at lower temperatures, oxidative etching is typically required to achieve regular etching pits.

than in MoS₂. Interestingly, a similar result was reported elsewhere^{S8} for SF₆ plasma etching of TMDs: the wagon wheel etching pits in WS₂ and WSe₂ had much higher anisotropy and sharpness as compared to MoS₂ and MoTe₂.

S6. Destabilizing effect of the topmost MoS₂ on the i-zz and the consequences for the etching pit shape

The flake's surface / topmost layer is an obvious disruptor of the i-zz. The top layer of the flake is least affected by any interlayer interactions. Therefore, it strives to form a triangular hole. Although complete single-layer-deep triangles were observed around hexagonal etching pits in MoS₂ multilayer flakes annealed in water steam at 700°C,^{S1} we could not find a complete triangle by either SEM or AFM. Instead, a triangle with rounded vertices is observed. It might be caused by slower kinetics of MoS₂ oxidation in H₂O₂ solution at 65°C compared to annealing in water steam at 700°C. The topmost layer can also be partially passivated before any nanofabrication due to oxidation by air, which is typical upon TMD nanostructures storage in an ambient atmosphere and can be detected by X-ray photoelectron spectroscopy^{S9}). When the top layer is etched in a triangle-like shape along its less stable \perp -zz directions, it uncovers the more stable \perp -zz directions of a second layer and facilitates the adsorption of oxidative species there. This might also affect the third layer, which again has less stable \perp -zz directions under the triangle-like etched topmost layer areas. As a result, the second layer is destabilized and excessively etched in its least favorable direction. To a lesser extent, this process is translated to a certain number of layers below. However, each even-numbered layer stabilizes the edge more and more, and finally, an undisturbed i-zz structure is formed. Hence, a hexagonal shape of the etching pit is developed far enough from the flake surface. This gradual stabilization process is reflected in a stepped structure near the **ES1**. Magnified micrographs (Fig. S4) show that many steps have edges that do not follow zigzag directions, *i.e.*, form other than 0°, 60°, or 120° angles with the

major hexagon edge. This may corroborate a low difference in stabilities of zigzag armchair edges in MoS₂ discussed above, which in turn can explain the tendency of etching pits in MoS₂ to various distortions. Note that such stepped structures were not observed or reported elsewhere for the etching pits in WS₂. On the other hand, the steps with unusual angles may indicate a more complex local interaction between the etching fronts on adjacent layers like in the model described in Ref.^{S10} Pinning of the etching fronts on the point defects of involved layers can also take place.

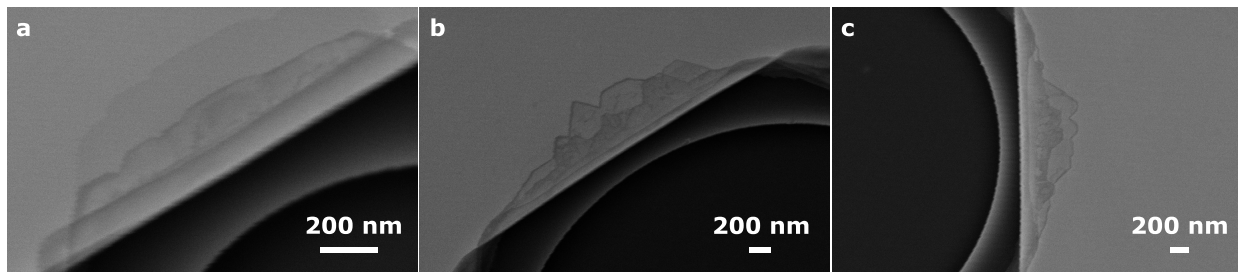


Figure S4: Magnified view of **ES1** structure near the 2 μm (a) and 5 μm (b,c) hexagons. The etched steps in the upper layers have edges that do not follow zigzag directions, *i.e.*, form other than 0° , 60° , or 120° angles with the major hexagon edge.

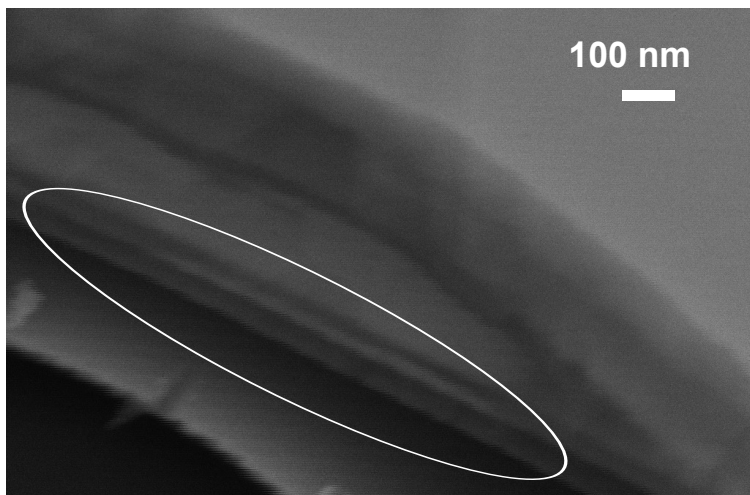


Figure S5: Magnified SEM view of the goffered structure of the hexagon wall formed by the bottom layers at **ES2** side of the 5 μm hexagon.

S7. Stacking faults and intergrown polytype domains in 2H-MoS₂

Being a van der Waals layered material, MoS₂ easily incorporates stacking faults and domains of different polytypes into both its natural and synthesized 3D crystals.^{S11,S12} The stacking fault in 2H-MoS₂ implies the inclusion of an S-Mo-S layer with the very same trigonal prismatic Mo coordination but with a shifted or rotated alignment of S and Mo sheets with respect to the normal A₁B₂ stacking sequence. Five stacking faults are possible upon one infraction to the stacking order of 2H-MoS₂.^{S11} The inclusion of more than one unusually stacked layer can be described as an intergrowth of another polytype within the 2H host domain.^{S12} The guest polytypes usually contain several consecutive S-Mo-S layers with parallel orientation^{S12} (*e.g.*, A₁B₁C₁ stacking). X-ray diffraction can characterize an average percentage of polytype intergrowth.^{S13} However, high-resolution STEM enables direct visualization of complex stacking sequences in MoS₂ crystals. Noteworthy, intergrown polytype domains with 3 to 7 parallel-oriented S-Mo-S layers were observed in natural 2H-MoS₂ microcrystals.^{S12} Several such guest domains can follow one another just in the 50 nm thick part of the crystal. The density of stacking faults in MoS₂ increases with more admixture atoms (like Re, Fe, Pb, etc.). Recently, 2H-MoS₂ crystals synthesized *via* a novel liquid salt transport method were claimed to have higher quality than commercially available ones synthesized by chemical vapor transport. Nevertheless, they still contained about 3% of polytype intergrowths with parallel stacking.^{S13} Therefore, the stacking faults and guest polytype domains are not unusual and may exist in MoS₂ flakes produced by mechanical exfoliation of commercially available 2H-MoS₂ crystals.

S8. Additional Raman spectroscopy maps of 2 μm hexagon

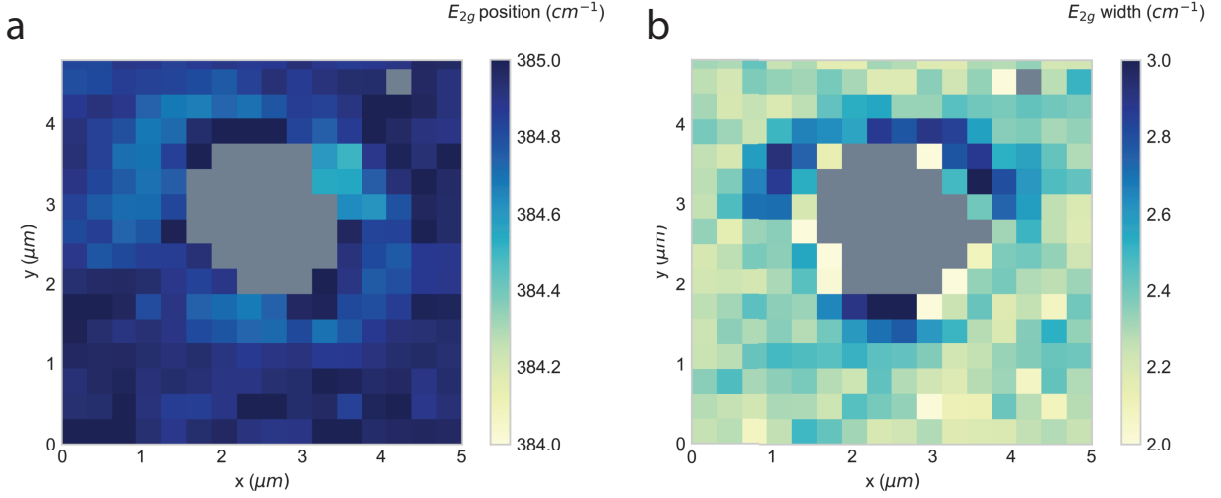


Figure S6: Raman maps of 2 μm hexagon in MoS_2 showing the spectral position (a) and FWHM (b) of the in-plane vibrational mode E_{2g} . This result is in line with the out-of-plane mode A_{1g} data shown in the Main text.

S9. SHG intensity derivation

The SHG setup described in the main text is suitable for measuring the intensity component parallel to the incoming laser excitation $I_{\parallel}(\theta)$. The reflection geometry follows the sequence:

$$\text{Laser} \xrightarrow{\text{LP}} E_{\omega} \xrightarrow{\lambda/2} E_{\omega}(\theta) \xrightarrow{\text{Sample}} P_{2\omega} \xrightarrow{\lambda/2} P_{2\omega}(-\theta) \xrightarrow{\text{LP}} I_{\parallel}(\theta)$$

Where black text denotes radiation going *towards* the sample, and red text denotes radiation that travels *from* the sample towards the detector. Note that every rotation is done by the $\lambda/2$ plate.

Following this sequence, we will follow the transformation of an incoming electric field with a fixed polarization along the \hat{x} direction, which is rotated by the $\lambda/2$ plate by an angle

θ through the rotation matrix $T(\theta)$. We assume a reflection geometry, and thus vanishing z components in the fields and the $\chi^{(2)}$ tensor-related elements.

$$E_\omega = \begin{pmatrix} 1 \\ 0 \end{pmatrix}; \quad T(\theta) = \begin{pmatrix} \cos\theta & -\sin\theta \\ \sin\theta & \cos\theta \end{pmatrix}; \quad R_\omega(\theta) = T(\theta)E_\omega \quad (\text{S2})$$

And by the definition of the $\chi^{(2)}$ tensor:

$$P_i(2\omega_0) = \epsilon_0 \sum_{jk} \chi_{ijk}^{(2)}(2\omega_0; \omega_0) E_j(\omega_0) E_k(\omega_0) \quad (\text{S3})$$

We obtain for the induced components at frequency 2ω out of the material:

$$\begin{aligned} P_{2\omega}(\theta) &= \begin{pmatrix} \chi_{xxx} R_\omega^x(\theta) R_\omega^x(\theta) + \chi_{xyy} R_\omega^y(\theta) R_\omega^y(\theta) + \chi_{xxy} R_\omega^x(\theta) R_\omega^y(\theta) + \chi_{xyx} R_\omega^y(\theta) R_\omega^x(\theta) \\ \chi_{yxx} R_\omega^x(\theta) R_\omega^x(\theta) + \chi_{yyx} R_\omega^x(\theta) R_\omega^y(\theta) + \chi_{yxy} R_\omega^y(\theta) R_\omega^x(\theta) + \chi_{yyy} R_\omega^y(\theta) R_\omega^y(\theta) \end{pmatrix} \\ &= \begin{pmatrix} \chi_{xxx} \cos^2\theta + (\chi_{xxy} + \chi_{xyx}) \cos\theta \sin\theta + \chi_{xyy} \sin^2\theta \\ \chi_{yxx} \cos^2\theta + (\chi_{yxy} + \chi_{yyx}) \cos\theta \sin\theta + \chi_{yyy} \sin^2\theta \end{pmatrix} \end{aligned} \quad (\text{S4})$$

Which, by performing a new rotation at the half-wave plate, we obtain $P'_{2\omega}(\theta') = T(-\theta)P_{2\omega}(\theta)$, and by applying Kleimann's symmetry conditions $\chi_{xxy}^{(2)} = \chi_{xyx}^{(2)} = \chi_{yxx}^{(2)}$ and $\chi_{xyy}^{(2)} = \chi_{yyx}^{(2)} = \chi_{yxy}^{(2)}$ we obtain:

$$P'_{2\omega}(\theta') = \begin{pmatrix} \chi_{xxx} \cos^3(\theta) + 3\chi_{xyy} \cos^2\theta \sin\theta + 3\chi_{xxy} \cos\theta \sin^2\theta + \chi_{yyy} \sin^3\theta \\ \chi_{yxx} \cos^3(\theta) + (2\chi_{yxy} - \chi_{xxx}) \cos^2\theta \sin\theta + (\chi_{yyy} - 2\chi_{xxy}) \cos\theta \sin^2\theta + \chi_{yxx} \sin^3\theta \end{pmatrix} \quad (\text{S5})$$

Which will in turn give us the parallel intensity by $I_{\parallel}(\theta) = |P'_{2\omega}(\theta')|^2$.

References

- [S1] Wang, Z.; Li, Q.; Xu, H.; Dahl-Petersen, C.; Yang, Q.; Cheng, D.; Cao, D.; Besenbacher, F.; Lauritsen, J. V.; Helveg, S. et al. Controllable etching of MoS₂ basal planes for enhanced hydrogen evolution through the formation of active edge sites. *Nano Energy* **2018**, *49*, 634–643.
- [S2] Yamamoto, M.; Einstein, T. L.; Fuhrer, M. S.; Cullen, W. G. Anisotropic Etching of Atomically Thin MoS₂. *J. Phys. Chem. C* **2013**, *117*, 25643–25649.
- [S3] Zhou, H.; Yu, F.; Liu, Y.; Zou, X.; Cong, C.; Qiu, C.; Yu, T.; Yan, Z.; Shen, X.; Sun, L. et al. Thickness-dependent patterning of MoS₂ sheets with well-oriented triangular pits by heating in air. *Nano Res.* **2013**, *6*, 703–711.
- [S4] Bala, A.; Sen, A.; Kim, Y.-H.; Kim, Y.-M.; Gandla, S.; Park, H.; Kim, S. Large-Area MoS₂ Nanosheets with Triangular Nanopore Arrays as Active and Robust Electrocatalysts for Hydrogen Evolution. *J. Phys. Chem. C* **2022**, *126*, 9696–9703.
- [S5] Huang, Z.; Deng, W.; Zhang, Z.; Zhao, B.; Zhang, H.; Wang, D.; Li, B.; Liu, M.; Huangfu, Y.; Duan, X. Terminal Atom-Controlled Etching of 2D-TMDs. *Adv. Mater.* **2023**, 2211252.
- [S6] Lucking, M. C.; Bang, J.; Terrones, H.; Sun, Y.-Y.; Zhang, S. Multivalency-induced band gap opening at MoS₂ edges. *Chem. Mater.* **2015**, *27*, 3326–3331.
- [S7] Munkhbat, B.; Yankovich, A. B.; Baranov, D. G.; Verre, R.; Olsson, E.; Shegai, T. O. Transition metal dichalcogenide metamaterials with atomic precision. *Nat. Commun.* **2020**, *11*, 4604.
- [S8] Danielsen, D. R.; Lyksborg-Andersen, A.; Nielsen, K. E. S.; Jessen, B. S.; Booth, T. J.; Doan, M.-H.; Zhou, Y.; Bøggild, P.; Gammelgaard, L. Super-Resolution Nanolithog-

- raphy of Two-Dimensional Materials by Anisotropic Etching. *ACS Appl. Mater. Interfaces* **2021**, *13*, 41886–41894.
- [S9] Polyakov, A. Y.; Kozlov, D. A.; Lebedev, V. A.; Chumakov, R. G.; Frolov, A. S.; Yashina, L. V.; Rumyantseva, M. N.; Goodilin, E. A. Gold Decoration and Photoresistive Response to Nitrogen Dioxide of WS₂ Nanotubes. *Chem. - Eur. J.* **2018**, *24*, 18952–18962.
- [S10] Fairbrother, J. A.; Cowan, M. D. Etch Pits in Natural Molybdenite. *J. Appl. Phys.* **1972**, *43*, 1366–1372.
- [S11] Bahl, O. P.; Evans, E. L.; Thomas, J. M. The identification and some properties of point defects and non-basal dislocations in molybdenite surfaces. *Proc. R. Soc. London, Ser. A* **1968**, *306*, 53–65.
- [S12] Yang, Y.; He, H.; Xian, H.; Xi, J.; Wu, X.; Chen, A.; Zhu, J.; Xu, H. Periodic and non-periodic stacking in molybdenite (MoS₂) revealed by STEM. *Am. Mineral.* **2022**, *107*, 997–1006.
- [S13] Cevallos, F. A.; Guo, S.; Heo, H.; Scuri, G.; Zhou, Y.; Sung, J.; Taniguchi, T.; Watanabe, K.; Kim, P.; Park, H. et al. Liquid Salt Transport Growth of Single Crystals of the Layered Dichalcogenides MoS₂ and WS₂. *Cryst. Growth Des.* **2019**, *19*, 5762–5767.